

Resolving Transient Electron-Phonon Coupling with Time-Resolved Spontaneous Raman Spectroscopy

Guy Reuveni,¹ Maya Levy Greenberg,¹ Matan Menahem,¹ Olle Hellman,^{2,*} and Omer Yaffe^{1,†}

¹*Department of Chemical and Biological Physics, Weizmann Institute of Science, Rehovot 7610001, Israel;*

²*Department of Molecular Chemistry and Material Science, Weizmann Institute of Science, Rehovot 7610001, Israel;*

(Dated: March 10, 2026)

Understanding the interaction of charge carriers with lattice vibrations in the quasi-equilibrium regime is crucial for semiconductor functionality. However, the structural signatures of these interactions are often too subtle for conventional ultrafast techniques to detect. We developed a time-resolved spontaneous Raman technique based on time-correlated single-photon counting to track the spectral response following photoexcitation, providing sub-wavenumber spectral resolution and a few-hundred-picosecond temporal resolution. Unlike traditional pump-probe schemes, our method utilizes a modulated continuous-wave probe to maintain high spectral resolution, enabling detection of low-frequency Raman shifts down to 10 cm^{-1} . Applied to lightly boron-doped silicon, we resolve *intra*-valence band and *inter*-valence band electronic transitions. A coupled-mode analysis of transient phonon asymmetry, resulting from interference with the inter-valence band transitions, reveals electron-phonon coupling parameters that directly relate to carrier recombination. By capturing these subtle dynamical shifts, we demonstrate that this platform offers a powerful probe for investigating electron-phonon interactions in long-lived excited states.

Keywords: Time-resolved Raman spectroscopy, Time-correlated single-photon counting, Quasi-equilibrium dynamics, Electron-phonon coupling, Silicon

INTRODUCTION

Following photoexcitation, hot carriers rapidly lose phase coherence and relax toward the band edges through carrier-carrier scattering and phonon emission on sub-picosecond timescales. After this initial relaxation, electrons and holes accumulate near the bottom of the conduction band and the top of the valence band, forming a quasi-equilibrium carrier distribution. The carrier population then gradually decreases through recombination over timescales ranging from picoseconds to microseconds^{1,2}. This quasi-equilibrium stage is central to material functionality. During this period, processes such as transport of free carriers or polarons, self-trapping, and exciton dissociation occur through interactions between electronic and structural degrees of freedom³⁻⁶.

Common ultrafast spectroscopies predominantly track interactions between electronic and structural degrees of freedom by monitoring observables related to electronic properties. Transient absorption and time-resolved photoluminescence follow carrier densities and band-structure evolution^{7,8}, while terahertz spectroscopy probes carrier mobility and scattering dynamics⁹. Coherent Raman techniques track impulsively driven vibrational modes, but their sensitivity diminishes once phase coherence is lost after a few picoseconds, limiting them largely to the hot-carrier cooling regime rather than the longer-lived quasi-equilibrium state¹⁰.

In contrast, time-resolved spontaneous Raman scattering directly probes vibrational and structural dynamics

throughout this quasi-equilibrium regime¹¹. The temporal evolution of Raman frequency, linewidth, and intensity encodes changes in force constants, phonon lifetimes, and mode populations^{12,13}. Because the Raman cross section depends on the electronic polarizability, the technique is inherently sensitive to transient modifications of electron-phonon coupling and local bonding¹⁴. It therefore provides direct access to how vibrational energy redistributes across the lattice and how electronic excitations reshape the structural landscape^{15,16}.

The common approach to time-resolved spontaneous Raman scattering is a pump-probe scheme. An ultrafast pump pulse drives the system out of equilibrium, and another, time-delayed ultrashort probe pulse records the spontaneous Raman response^{11-13,15,17-27}. Clearly, the use of ultrashort pulses limits the spectral resolution of the Raman spectra. In principle, pump-probe Raman experiments can achieve high spectral resolution by using long probe pulses with narrow bandwidth. In practice, this is uncommon and even when the probe pulse is long and spectrally narrow, amplified spontaneous emission and residual spectral wings near the laser line make efficient filtering difficult¹¹. These issues become especially severe when probing low-frequency Raman shifts below $\sim 100\text{ cm}^{-1}$, where strong suppression of stray light is required.

Here we implement an alternative approach to time-resolved Raman scattering based on time-correlated single-photon counting (TCSPC), in which individual Raman photons are time-tagged relative to the pump excitation²⁸⁻³⁰. By combining a modulated continuous-wave probe with TCSPC detection and a pulsed optical pump, we obtain a few-hundred-picosecond temporal resolution while maintaining high spectral resolution. We demonstrate this approach in silicon, where photoex-

* olle.hellman@weizmann.ac.il

† omer.yaffe@weizmann.ac.il

citation induces two Raman-active valence-band transitions. An *intra-valence-band* (intra-VB) transitions appears at low shifts up to 200 cm^{-1} ^{31–34}, while an *inter-valence-band* (inter-VB) transitions overlaps with the optical phonon at 521 cm^{-1} , creating an asymmetric Fano lineshape ^{7,11,13,35,38}. High spectral resolution enables a coupled-mode analysis to extract electron–phonon coupling parameters, which track the photoexcited carrier density during recombination.

RESULTS AND DISCUSSION

TCSPC-Based Time-Resolved Raman Experimental Platform

Time-resolved spontaneous Raman scattering measurements are performed using a setup based on TCSPC detection, schematically shown in Fig. 1(a). The instrument is built around a 1 m focal-length monochromator equipped with a $1800 \text{ grooves mm}^{-1}$ grating. The spectrometer is coupled to an optical microscope operating in a back-scattering configuration. A continuous-wave diode laser provides probe excitation at 785 nm. An acousto-optic modulator amplitude-modulates the probe beam at 20 kHz to generate an on-off sequence, enabling subtraction of pump-induced photoluminescence from the Raman signal. Non-equilibrium dynamics are initiated by a spatially co-aligned pulsed optical pump centered at 515 nm. The pump delivers 64 ps pulses with an energy of 2.3 nJ at a repetition rate of 10 MHz, corresponding to a fluence of approximately 70 mJ cm^{-2} . Elastic scattering from the excitation line is suppressed using a beam splitter in combination with two volume holographic grating notch filters, enabling detection of low-frequency Raman shifts down to 10 cm^{-1} .

The spectrally dispersed Raman signal is collected at the monochromator’s exit slit and detected by a single-photon avalanche photodiode (SPAD). Photon arrival times are recorded with a time-tagging module, with synchronization between the laser sources, modulation electronics, and detection system provided by a pulse generator. The overall temporal instrument response function, determined by the timing jitter of the spectrometer, detector, time tagger, and associated electronics, has a full width at half maximum of approximately 600 ps. A time-resolved Raman spectrum is obtained by sequentially scanning the monochromator grating. At each spectral position, TCSPC is used to accumulate a temporal histogram of Raman photon arrival times, from which the full time- and frequency-resolved Raman response is reconstructed.

The temporal instrument response function does not represent a fundamental limitation of the method. Improved temporal resolution is expected with state-of-the-art low-jitter avalanche photodiode arrays, which would also enable operation in spectrograph mode, thereby significantly reducing the acquisition time for a full spec-

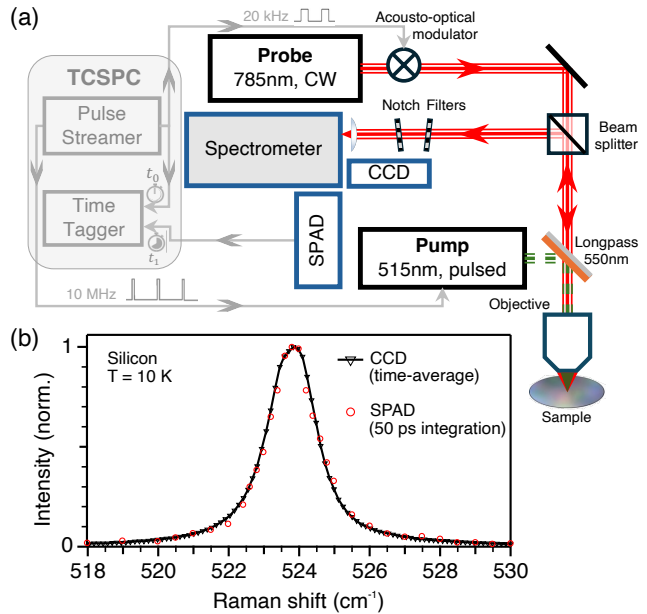


FIG. 1. (a) Schematic of the time-resolved spontaneous Raman spectroscopy apparatus utilizing time-correlated single-photon counting. A modulated continuous-wave probe at 785 nm and a pulsed pump at 515 nm are co-aligned onto the sample. (b) Normalized probe-only Raman spectra of the silicon optical phonon at 10 K are recorded using a CCD detector (black) and reconstructed from a single 50 ps time bin using the single-photon avalanche photodiode with TCSPC (red). The overlap demonstrates that introducing picosecond time resolution does not compromise spectral resolution.

trum ^{39,40}. Additional improvements are anticipated with advanced time-tagging electronics and shorter pump pulse durations. Figure 1(b) demonstrates that a spectrum reconstructed within a 50 ps temporal window retains the same spectral resolution as a time-averaged charge-coupled device (CCD) measurement. The silicon optical phonon is measured at 10 K under probe-only illumination, where its narrow linewidth provides a stringent test of spectral performance.

Electronic and Phonon Dynamics in Photoexcited Silicon

To demonstrate the capabilities of high-resolution time-resolved spontaneous Raman spectroscopy, we study the dynamics of photoexcitation of lightly boron-doped silicon wafer (dopant concentration $1 \cdot 10^{14} \text{ cm}^{-3}$) with a native oxide layer as a model system.

Figure 2(a) displays the Stokes and anti-Stokes transient Raman response for an estimated excess carrier density of approximately $5 \cdot 10^{18} \text{ cm}^{-3}$ during the first 0.5 ns after excitation at 280 K (refer to the Supplementary Information for similar data across a temperature range of 10 to 280 K). In the top panel, the spectrum before excitation (shown in red and averaged over the interval

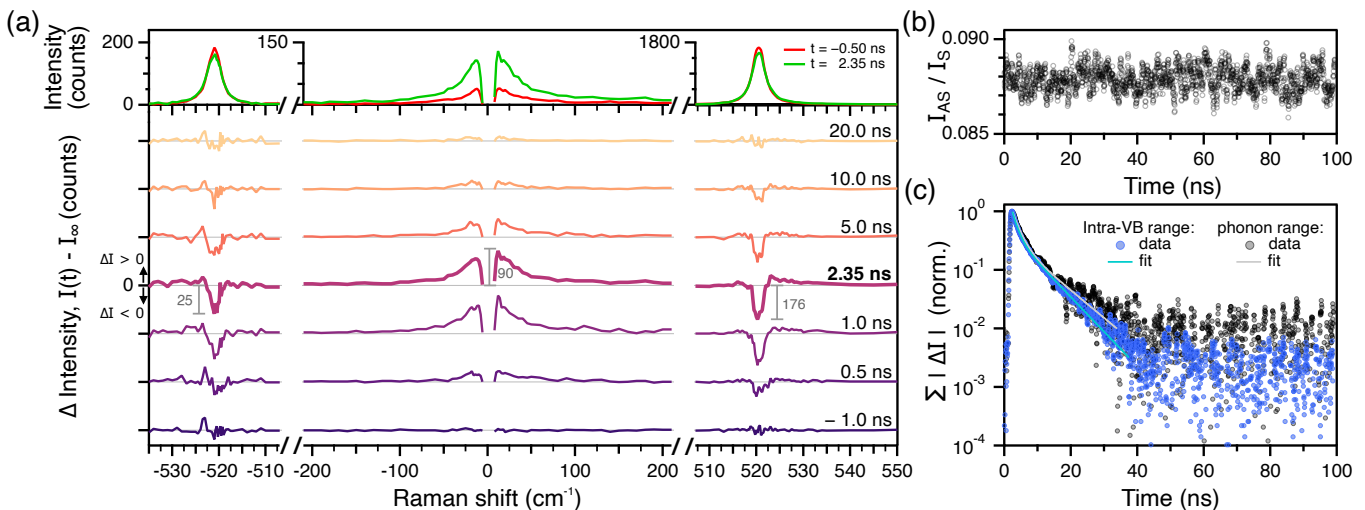


FIG. 2. Time-resolved spontaneous Raman response of lightly boron-doped silicon at 280 K. (a) Top panel: Raman spectrum of low-doped silicon pre-excitation (red) and post-excitation (green). Bottom panel: Differential spectra $\Delta I(\omega, t)$ obtained by subtracting the pre-excitation spectrum from each transient spectrum. The bold spectrum at $t = 2.35$ ns represents the maximum distortion. Differential spectra are offset for clarity, with gray axes indicating the zero level and gray scale bars representing the ΔI magnitude for each spectral range. The data reveal a transient amplification of the low-frequency *intra-valence-band* (intra-VB) signal and a time-dependent modification of the optical phonon near 521 cm^{-1} due to the *inter-valence-band* (inter-VB) transitions. (b) Time-dependent anti-Stokes/Stokes amplitude ratio. The constant ratio verifies that no significant lattice heating occurs during the measurement. (c) Temporal evolution of the normalized integrated absolute differential intensity $\sum_{\omega} |\Delta I|$, integrated over the intra-VB ($10\text{--}200 \text{ cm}^{-1}$, blue) and phonon ($510\text{--}560 \text{ cm}^{-1}$, black) spectral ranges, shown with bi-exponential fits.

from -0.5 to 0 ns) is compared with the spectrum averaged over the period from 2.35 to 2.85 ns after excitation (shown in green). The bottom panel presents the differential spectra $\Delta I(\omega, t) = I(\omega, t) - I_{\infty}$, where I_{∞} refers to the spectrum prior to excitation. The most significant distortion occurs at $t = 2.35$ ns, revealing two correlated features: a broad low-frequency Raman scattering signal that extends to approximately 200 cm^{-1} , and a marked modification of the zone-center optical phonon at 521 cm^{-1} .

The low-frequency response arises from intra-VB transitions of holes in the valence band of silicon, occurring at low Raman shifts up to approximately 200 cm^{-1} ^{31–34}. Concurrently, a continuum of inter-VB hole transitions begins near 355 cm^{-1} and extends to higher energies, overlapping with the optical phonon at 521 cm^{-1} ^{7,11,13,35,38,41}. The interference between these transitions and the discrete phonon transition produces the characteristic asymmetric transient Fano lineshape.

Figure 2(b) demonstrates that these spectral changes are not caused by lattice heating. The anti-Stokes/Stokes amplitude ratio, which provides direct lattice thermometry ^{11,25,42,43}, remains constant within experimental uncertainty, indicating that the lattice temperature does not increase during the transient response. Figure 2(c) shows the temporal evolution of the normalized, integrated absolute differential intensity, $\sum_{\omega} |\Delta I(\omega, t)|$, evaluated over the intra-VB Raman range ($10\text{--}200 \text{ cm}^{-1}$, blue) and the phonon range ($510\text{--}560 \text{ cm}^{-1}$, black). The latter is assigned to the optical phonon, the inter-VB

transitions, and their mutual interference. Both signals rise promptly after photoexcitation and decay toward equilibrium, tracking the transient carrier population via a bi-exponential decay typical of carrier recombination in silicon ^{44–46}. Focusing on the dominant fast component, we extract decay constants of $\tau_1 = 1.8$ ns for the intra-VB signal and $\tau_1 = 2.7$ ns for the phonon feature. While these values differ, they are of the same order of magnitude and are consistent with effective carrier lifetimes in lightly doped silicon with a native oxide, where surface recombination dominates ⁴⁷.

Transient Electron–Phonon Interactions

Next, we turn to the additional information encoded in the transient Raman lineshape, which becomes accessible owing to the high spectral resolution of the present measurements. We focus on the optical phonon and the associated inter-VB region, as the low-frequency intra-VB electronic response is spectrally broad and featureless, thus precluding a meaningful decomposition into distinct components.

Although the asymmetric phonon peak in the presence of photoexcited carriers is often described within the Fano formalism, we do not adopt that approach here. In the conventional Fano model, the discrete excitation is treated as a stationary eigenstate whose spectral width arises solely from its interaction with a continuum of elec-

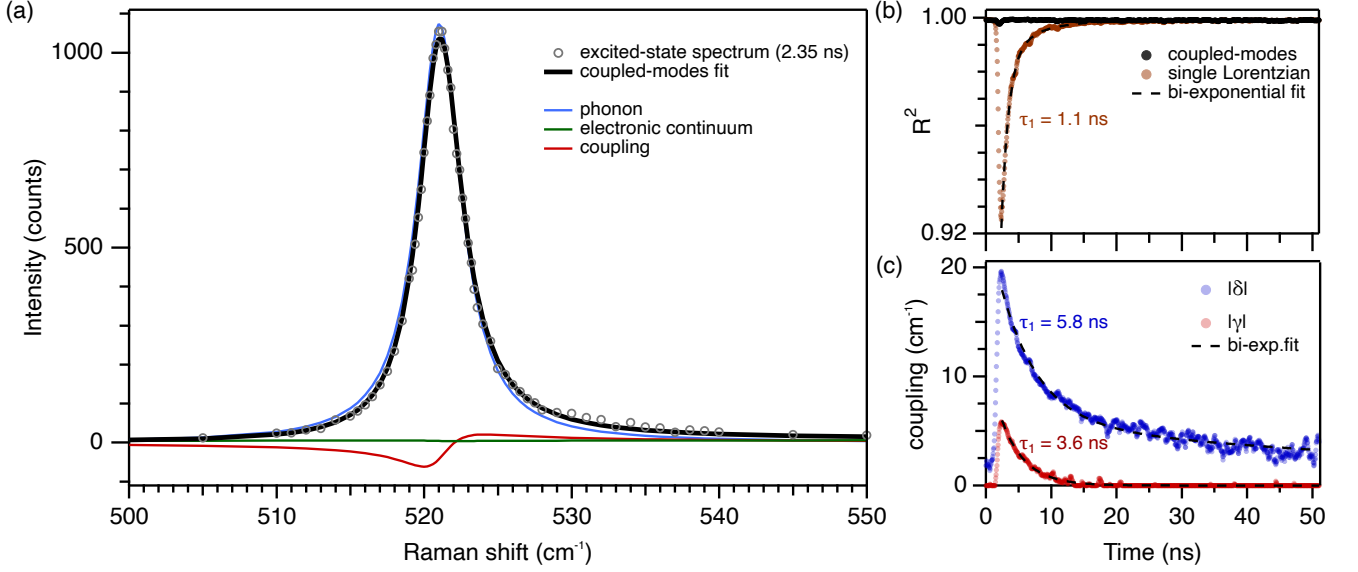


FIG. 3. Time-resolved lineshape analysis of the optical phonon and the *inter*-valence-band (inter-VB) spectral region in lightly boron-doped silicon at 280 K. (a) Raman spectrum 2.35 ns after photoexcitation. Gray circles indicate the time-averaged spectrum integrated over 2.35–2.85 ns, shown alongside the two-coupled-modes fit (black). The asymmetry of the peak is apparent compared to the purely phononic contribution (blue), with most of the asymmetry originating from the cross terms (red) between the inter-VB transitions and the phonon. The direct contribution from the inter-VB electronic transitions (green) is negligible. (b) Statistical R^2 for the coupled-mode fit (black), compared with a single Lorentz oscillator fit (brown). (c) Temporal evolution of the absolute real ($|\delta|$, blue) and imaginary ($|\gamma|$, red) coupling parameters. The dashed curves in (b) and (c) represent bi-exponential fits to the transients.

tronic transitions⁵. Within this framework, the phonon linewidth is rigidly tied to the strength of the coupling to the inter-VB transitions and does not account for the intrinsic phonon lifetime, which exists independently of the electronic continuum and exhibits a pronounced temperature dependence (see Supplementary Information). Moreover, the Fano formalism is constructed to diagonalize the energy matrix of stationary states and does not natively describe the time-dependent evolution of a coupled system. In our measurements, the phonon lineshape evolves continuously from an asymmetric profile shortly after excitation to a nearly symmetric form at longer delay times as the carrier population decays. This transient relaxation of the spectral asymmetry cannot be captured by a model based solely on static energy eigenvalues.

Instead, we employ a general description based on two coupled Lorentzian modes⁴⁹, consisting of a narrow mode representing the optical phonon and a broad mode representing the inter-VB transitions. This approach separates intrinsic phonon lifetime effects from coupling-induced distortions and provides a unified framework for analyzing the temporal dependence of the spectra. Formally, the system is described by a Green's function $G(\Omega)$ ¹², as previously implemented for coupled-mode systems^{51–53}. The Raman intensity is proportional to the corresponding spectral function, given by the imaginary part of the Green's function weighted by the Raman po-

larizability derivatives,

$$I(\omega, T) \propto n(\omega, T) \sum_{ij} [-\text{Im}\{G_{ij}(\omega, T)\} \chi_i \chi_j], \quad (1)$$

where χ_1 and χ_2 denote the polarizability derivatives associated with the phonon and the inter-VB transitions, respectively. The interacting Green's function follows from the Dyson equation,

$$G(\Omega)^{-1} = g^0(\Omega)^{-1} + \Sigma(\Omega), \quad (2)$$

where $g^0(\Omega)$ is the harmonic Green's function and $\Sigma(\Omega)$ is the self-energy. For two coupled modes with frequency-independent parameters^{51,52}, these matrices take the form

$$g^0(\Omega)^{-1} = \begin{pmatrix} \omega_1^2 - \Omega^2 & 0 \\ 0 & \omega_2^2 - \Omega^2 \end{pmatrix}, \quad (3)$$

$$\Sigma(\Omega, t) = \Omega \begin{pmatrix} -i\Gamma_1 & \delta(t) + i\gamma(t) \\ \delta(t) + i\gamma(t) & -i\Gamma_2 \end{pmatrix}. \quad (4)$$

Here Ω is the probing frequency, ω_1 and ω_2 are the bare frequencies of the phonon and inter-VB transitions mode, Γ_1 and Γ_2 are their respective damping constants, and $\delta(t)$ and $\gamma(t)$ represent the real and imaginary parts of the time-dependent intermode coupling.

To ensure physical robustness and avoid over-

parameterization, we impose several constraints in the fitting procedure. The central frequency and width of the inter-VB transitions are fixed at $\omega_2 = 700 \text{ cm}^{-1}$ and $\Gamma_2 = 400 \text{ cm}^{-1}$, reflecting the broad inter-VB Raman response of silicon that overlaps the optical phonon near 521 cm^{-1} ^{11,41}. The relatively modest phonon spectral distortion induced by photoexcitation supports keeping these parameters constant throughout the transient. The inter-VB transitions scattering strength χ_2 is fixed at 20, as the fits are not sensitive to its precise value. The phonon frequency ω_1 , damping Γ_1 , and scattering strength χ_1 are fixed to the Lorentzian parameters extracted from the spectrum prior to the excitation. This procedure assumes that the transient modifications arise from coupling to the inter-VB transitions rather than from changes in the intrinsic phonon lifetime.

Under these constraints, the only free parameters are the coupling terms $\delta(t)$ and $\gamma(t)$. Physically, both are expected to scale with the photoexcited carrier concentration, since the effective electron-phonon interaction strength is proportional to the density of free carriers. We therefore treat them as time-dependent quantities that implicitly incorporate the carrier population. The real part δ couples the mode frequencies, while the imaginary part γ couples their damping channels and represents a dissipative interaction ⁵⁴.

The results of this analysis are summarized in Fig. 3. Panel (a) shows the coupled-modes fit to the excited-state spectrum, 2.35 nanoseconds after excitation, when the photoexcitation effect peaks. The cross term between the phonon and inter-VB transitions, shown in red, dominates the asymmetry, whereas the direct contribution of the inter-VB transitions (green) is negligible. Panel (b) presents the statistical R^2 of the coupled-mode fit, compared with that of a simple Lorentz oscillator model. The superior performance of the coupled-mode description highlights the transient contribution of the coupling to the inter-VB transitions and its temporal decay, demonstrating that the coupled-mode model is required to reproduce the asymmetric phonon profile. Panel (c) shows the temporal evolution of $\delta(t)$ and $\gamma(t)$. Dashed curves in (b) and (c) are the bi-exponential function fits to the transients.

The extracted decay constants (τ_1) for $R^2(t)$, $\delta(t)$, and $\gamma(t)$ are not identical. This deviation from a single scaling factor reflects the fact that δ and γ enter the Raman intensity expression in eq. (1) with different functional dependence, and the statistical measure R^2 is not expected to vary linearly with carrier concentration. Nevertheless, the overall agreement in their temporal behavior supports the interpretation that the transient lineshape evolution is governed by the decay of the photoexcited carrier population.

In summary, high-resolution time-resolved spontaneous Raman spectroscopy reveals the dynamics of electron-phonon interactions in photoexcited silicon dur-

ing the quasi-equilibrium regime. A coupled-mode analysis shows that the transient asymmetry of the optical phonon arises from its time-dependent interaction with the inter-VB transitions. The coupling parameters $\delta(t)$ and $\gamma(t)$ quantify how the photoexcited carrier population modifies the phonon properties, and their decay directly follows the reduction of the carrier density during recombination.

CONCLUSIONS

Our work addresses the challenge of resolving the subtle interactions between charge carriers and lattice vibrations during the quasi-equilibrium regime of semiconductors. By implementing a time-correlated single-photon counting (TCSPC) approach with a modulated continuous-wave probe, we achieve sub-wavenumber spectral resolution and a few-hundred-picosecond temporal resolution. This allows for the detection of low-frequency shifts and high-frequency phonon modifications. We demonstrated the effectiveness of this technique in lightly boron-doped silicon, resolving the transient amplification of the *intra*-valence-band transitions and the time-dependent interference between the optical phonon and the *inter*-valence-band transitions. Using a coupled-mode analysis, we extracted time-dependent coupling parameters, $\delta(t)$ and $\gamma(t)$, which directly track the carrier recombination dynamics. This experimental platform offers a versatile high-resolution probe for investigating the complex electron-phonon interactions that define the functional properties of modern semiconductors.

Author Contributions

O.Y. and G.R. conceived the study. G.R. and M.L.G. developed the optical setup and performed the measurements. G.R. carried out the data analysis. O.H. developed the theoretical models. M.M. contributed to the setup development and numerical implementation of the fitting procedures. O.Y. supervised all stages of the project. All authors contributed to the interpretation of the results and to the final manuscript.

Acknowledgments

The authors thank Yehiam Prior and Maor Asher for their insightful feedback and Lior Segev for software development. G.R. and M.L.G. acknowledge support for this research by the Institute for Environmental Sustainability of the Weizmann Institute of Science. O.Y. acknowledges funding from the European Research Council (850041 — ANHARMONIC).

- [1] J. Shah, Initial relaxation of photoexcited carriers, in *Ultrafast Spectroscopy of Semiconductors and Semiconductor Nanostructures*, Springer Series in Solid-State Sciences (Springer, Berlin, Heidelberg, 1999) pp. 133–160.
- [2] R. Binder and S. W. Koch, Nonequilibrium semiconductor dynamics, *Progress in Quantum Electronics* **19**, 307 (1995).
- [3] P. T. Landsberg, *Recombination in semiconductors* (Cambridge University Press, Cambridge, 1991).
- [4] Y. Toyozawa, Optical spectra of exciton in the phonon field, in *Optical Processes in Solids* (Cambridge University Press, United Kingdom, 2003) pp. 192–238.
- [5] Y. Toyozawa, Polarons and the self-trapped state, in *Optical Processes in Solids* (Cambridge University Press, United Kingdom, 2003) pp. 149–191.
- [6] Y. Toyozawa, Photo-induced structural changes, in *Optical Processes in Solids* (Cambridge University Press, United Kingdom, 2003) pp. 319–370.
- [7] K. E. Knowles, M. D. Koch, and J. L. Shelton, Three applications of ultrafast transient absorption spectroscopy of semiconductor thin films: spectroelectrochemistry, microscopy, and identification of thermal contributions, *Journal of Materials Chemistry C* **6**, 11853 (2018).
- [8] T. Kirchartz, J. A. Márquez, M. Stolterfoht, and T. Unold, Photoluminescence-based characterization of halide perovskites for photovoltaics, *Advanced Energy Materials* **10**, 1904134 (2020).
- [9] T. Moriyasu, M. Tani, H. Kitahara, T. Furuya, J. Afalla, T. Kohmoto, D. Koide, H. Sato, and M. Kumakura, Photocarrier dynamics in thick Si film studied by optical pump-terahertz probe spectroscopy, *Optics Communications* **554**, 130139 (2024).
- [10] J. Shah, Coherent spectroscopy of semiconductors, in *Ultrafast Spectroscopy of Semiconductors and Semiconductor Nanostructures*, Springer Series in Solid-State Sciences (Springer, Berlin, Heidelberg, 1999) pp. 27–131.
- [11] R. B. Versteeg, J. Zhu, P. Padmanabhan, C. Boguschewski, R. German, M. Goedecke, P. Becker, and P. H. M. Van Loosdrecht, A tunable time-resolved spontaneous Raman spectroscopy setup for probing ultrafast collective excitation and quasiparticle dynamics in quantum materials, *Structural Dynamics* **5**, 044301 (2018).
- [12] J. A. Kash, J. C. Tsang, and J. M. Hvam, Subpicosecond time-resolved Raman spectroscopy of LO phonons in GaAs, *Physical Review Letters* **54**, 2151 (1985).
- [13] J. Zhu, R. B. Versteeg, P. Padmanabhan, and P. H. M. Van Loosdrecht, Dynamical resonance quench and Fano interference in spontaneous Raman scattering from quasiparticle and collective excitations, *Physical Review B* **99**, 094305 (2019).
- [14] D. L. Mills, A. A. Maradudin, and E. Burstein, Theory of the Raman effect in metals, *Annals of Physics* **56**, 504 (1970).
- [15] A. M. Finardi, C. Fasolato, A. Giugni, M. Capecchia, R. Cucini, E. Cappelluti, F. Sacchetti, G. Panaccione, P. Postorino, C. Petrillo, and G. Rossi, Transient photodoping and phonon dynamics in bulk and monolayer MoS₂ by time resolved Raman scattering, *npj 2D Materials and Applications* **9**, 79 (2025).
- [16] Z. Dai, C. Lian, J. Lafuente-Bartolome, and F. Giustino, Excitonic polarons and self-trapped excitons from first-principles exciton-phonon couplings, *Physical Review Letters* **132**, 036902 (2024).
- [17] S. Han, C. Boguschewski, Y. Gao, L. Xiao, J. Zhu, and P. H. M. van Loosdrecht, Incoherent phonon population and exciton-exciton annihilation dynamics in monolayer WS₂ revealed by time-resolved resonance Raman scattering, *Optics Express* **27**, 29949 (2019).
- [18] J. Zhu, R. German, B. V. Senkovskiy, D. Haberer, F. R. Fischer, A. Grüneis, and P. H. M. Van Loosdrecht, Exciton and phonon dynamics in highly aligned 7-atom wide armchair graphene nanoribbons as seen by time-resolved spontaneous Raman scattering, *Nanoscale* **10**, 17975 (2018).
- [19] N. Pellatz, S. Roy, J. W. Lee, J. L. Schad, H. Kandel, N. Arndt, C. B. Eom, A. F. Kemper, and D. Reznik, Relaxation timescales and electron-phonon coupling in optically pumped YBa₂Cu₃O_{6+x} revealed by time-resolved Raman scattering, *Physical Review B* **104**, L180505 (2021).
- [20] K. Kang, T. Ozel, D. G. Cahill, and M. Shim, Optical phonon lifetimes in single-walled carbon nanotubes by time-resolved Raman scattering, *Nano Letters* **8**, 4642 (2008).
- [21] H. Yugami, S. Nakashima, Y. Oka, M. Hangyo, and A. Mitsuishi, Time-resolved Raman scattering measurement of photoexcited plasmon in GaP crystals, *Journal of Applied Physics* **60**, 3303 (1986).
- [22] D. Y. Oberli, D. R. Wake, M. V. Klein, J. Klem, T. Henderson, and H. Morkoç, Time-resolved Raman scattering in GaAs quantum wells, *Physical Review Letters* **59**, 696 (1987).
- [23] H. Yan, D. Song, K. F. Mak, I. Chatzakis, J. Maultzsch, and T. F. Heinz, Time-resolved Raman spectroscopy of optical phonons in graphite: Phonon anharmonic coupling and anomalous stiffening, *Physical Review B* **80**, 121403 (2009).
- [24] J. A. Kash, S. S. Jha, and J. C. Tsang, Picosecond Raman studies of the Fröhlich interaction in semiconductor alloys, *Physical Review Letters* **58**, 1869 (1987).
- [25] T. H. Chou, M. Först, M. Fechner, M. Henstridge, S. Roy, M. Buzzi, D. Nicoletti, Y. Liu, S. Nakata, B. Keimer, and A. Cavalleri, Ultrafast Raman thermometry in driven YBa₂Cu₃O_{6.48}, *Physical Review B* **109**, 195141 (2024).
- [26] G. Raciti, B. Abad, R. Dettori, R. Sen, A. K. Sivan, J. M. Sojo-Gordillo, N. Vast, R. Ruruli, C. Melis, J. Sjakste, *et al.*, Unraveling energy flow mechanisms in semiconductors by ultrafast spectroscopy: Ge as a case study, *Advanced Science* , e15470 (2025).
- [27] K. Katsumi, A. Alekhin, S. M. Souliou, M. Merz, A. A. Haghighirad, M. Le Tacon, S. Houver, M. Cazayous, A. Sacuto, and Y. Gallais, Disentangling lattice and electronic instabilities in the excitonic insulator candidate Ta₂NiSe₅ by nonequilibrium spectroscopy, *Physical Review Letters* **130**, 106904 (2023).
- [28] F. Madonini and F. Villa, Single photon avalanche diode arrays for time-resolved Raman spectroscopy, *Sensors* **21**, 4287 (2021).
- [29] N. Finlayson, A. Usai, G. E. Brown, H. McEwan, A. T. Erdogan, C. J. Campbell, and R. K. Henderson, Time-correlated single photon Raman spectroscopy at megahertz repetition rates, *Optics Letters* **46**, 4104 (2021).

- [30] M. Kögler and B. Heilala, Time-gated Raman spectroscopy – a review, *Measurement Science and Technology* **32**, 012002 (2020).
- [31] K. Jain, S. Lai, and M. V. Klein, Electronic Raman scattering and the metal-insulator transition in doped silicon, *Physical Review B* **13**, 5448 (1976).
- [32] M. Chandrasekhar, M. Cardona, and E. O. Kane, Intra-band Raman scattering by free carriers in heavily doped n-Si, *Physical Review B* **16**, 3579 (1977).
- [33] M. Chandrasekhar, U. Rössler, and M. Cardona, Intra- and interband Raman scattering by free carriers in heavily doped p-Si, *Physical Review B* **22**, 761 (1980).
- [34] G. Abstreiter, M. Cardona, and A. Pinczuk, Light scattering by free carrier excitations in semiconductors, in *Light Scattering in Solids IV: Electronics Scattering, Spin Effects, SERS, and Morphic Effects* (Springer, Berlin, Heidelberg, 2005) pp. 5–150.
- [35] F. Cerdeira and M. Cardona, Effect of carrier concentration on the Raman frequencies of Si and Ge, *Physical Review B* **5**, 1440 (1972).
- [11] F. Cerdeira, T. A. Fjeldly, and M. Cardona, Effect of free carriers on zone-center vibrational modes in heavily doped p-type Si. II. optical modes, *Physical Review B* **8**, 4734 (1973).
- [7] F. Cerdeira, T. A. Fjeldly, and M. Cardona, Interaction between electronic and vibronic Raman scattering in heavily doped silicon, *Solid State Communications* **13**, 325 (1973).
- [38] M. Jouanne, M. A. Kanehisa, J. F. Morhange, N. M. Ravindra, and M. Balkanski, Bound state energy and line width due to the resonant interaction between optical phonon and electronic transitions in degenerate silicon, *Solid-State Electronics* **28**, 39 (1985).
- [39] I. Nissinen, J. Nissinen, P. Keränen, D. Stoppa, and J. Kostamovaara, A 16×256 SPAD line detector with a 50-ps, 3-bit, 256-channel time-to-digital converter for Raman spectroscopy, *IEEE Sensors Journal* **18**, 3789 (2018).
- [40] C. S. Tye, A. Kufcsák, C. A. Ross, K. Ehrlich, R. K. Henderson, and M. G. Tanner, Time-resolved Raman spectroscopy using a CMOS SPAD array to remove fluorescent and fibre Raman backgrounds, *Biomedical Optics Express* **16**, 2824 (2025).
- [41] M. A. Kanehisa, R. F. Wallis, and M. Balkanski, Inter-band electronic Raman scattering in p-silicon, *Physical Review B* **25**, 7619 (1982).
- [42] S. L. Cooper, P. Abbamonte, N. Mason, C. S. Snow, M. Kim, H. Barath, J. F. Karpus, C. E. Chialvo, J. P. Reed, Y.-I. Joe, *et al.*, Raman scattering as a tool for studying complex materials, in *Optical Techniques for Solid-State Materials Characterization* (CRC Press Boca Raton, Florida, 2012) pp. 193–236.
- [43] A. Compaan and H. J. Trodahl, Resonance Raman scattering in Si at elevated temperatures, *Physical Review B* **29**, 793 (1984).
- [44] Z. Li, A. Liu, R. Basnet, L. E. Black, D. Macdonald, and H. T. Nguyen, Applications of time-resolved photoluminescence for characterizing silicon photovoltaic materials, *Semiconductor Science and Technology* **40**, 045015 (2025).
- [45] M. Ghezellou, P. Kumar, M. E. Bathen, R. Karsthof, E. Ö. Sveinbjörnsson, U. Grossner, J. P. Bergman, L. Vines, and J. Ul-Hassan, The role of boron related defects in limiting charge carrier lifetime in 4H-SiC epitaxial layers, *APL Materials* **11**, 031107 (2023).
- [46] J. Dziejwior and W. Schmid, Auger coefficients for highly doped and highly excited silicon, *Applied Physics Letters* **31**, 346 (1977).
- [47] T. Markvart and L. Castañer, Chapter IA-2 - semiconductor materials and modelling, in *Solar Cells (Second Edition)* (Elsevier, 2013) pp. 27–54.
- [5] U. Fano, Effects of configuration interaction on intensities and phase shifts, *Physical Review* **124**, 1866 (1961).
- [49] J. F. Scott, Soft-mode spectroscopy: experimental studies of structural phase transitions, *Rev. Mod. Phys.* **46**, 83 (1973).
- [12] P. C. K. Kwok, Green’s function method in lattice dynamics, in *Solid State Physics*, Vol. 20 (Elsevier, 1968) pp. 213–303.
- [51] Y. Takagi, Coupled modes analysis of Raman spectra: Application to the case of a KH_2PO_4 crystal in the paraelectric phase, *Ferroelectrics* **46**, 245 (1983).
- [52] N. Benshalom, M. Asher, R. Jouclas, R. Korobko, G. Schweicher, J. Liu, Y. Geerts, O. Hellman, and O. Yaffe, Phonon–phonon interactions in the polarization dependence of Raman scattering, *Journal of Physical Chemistry C* **127**, 18099 (2023).
- [53] N. Pinsk, N. Benshalom, M. Hartstein, Y. Diskin-Posner, M. Menahem, O. Hellman, L. Kronik, and O. Yaffe, Hydrogen bonds induce double-well spectroscopic signatures in α -glycine, *Journal of the American Chemical Society* **147**, 41699 (2025).
- [54] A. S. Barker and J. J. Hopfield, Coupled-optical-phonon-mode theory of the infrared dispersion in BaTiO_3 , SrTiO_3 , and KTaO_3 , *Phys. Rev.* **135**, A1732 (1964).

Supplementary Information

Resolving Transient Electron-Phonon Coupling with Time-Resolved Spontaneous Raman Spectroscopy

Guy Reuveni,¹ Maya Levy Greenberg,¹ Matan Menahem,¹ Olle Hellman,^{2,*} and Omer Yaffe^{1,†}

¹*Department of Chemical and Biological Physics,*

Weizmann Institute of Science, Rehovot 7610001, Israel;

²*Department of Molecular Chemistry and Material Science,*

Weizmann Institute of Science, Rehovot 7610001, Israel;

(Dated: March 10, 2026)

* olle.hellman@weizmann.ac.il

† omer.yaffe@weizmann.ac.il

S1. EXPERIMENTAL

S1.a. TCSPC Time-Resolved Raman Experimental Platform

The time-resolved Raman scattering measurements were carried out using a setup developed by extending our existing high-resolution Raman platform^{S1,S2} (Figure 1 in the main article). The system is built around a 1 m focal-length monochromator (FHR 1000, Horiba), with a 1800 grooves mm^{-1} grating. The Raman probe laser is a 785 nm continuous-wave diode laser (XTRA II, Toptica Inc., USA), which is spectrally cleaned with amplified spontaneous emission filters and subsequently spatially filtered. The probe beam is directed into an acousto-optical modulator (M1206-P110L-1, ISOMET), where the first order, amplitude-modulated diffracted beam is taken downstream towards the sample, producing an on/off sequence at 20 kHz. The 515 nm pulsed pump laser (LDH-P-FA-515L, PicoQuant) with 2.3 nJ, 64 ps pulses at 10 MHz is passed through a telescope to ensure that the pump and probe focal points are precisely overlapping at the sample surface. The pump beam is then merged with the central optical path via a dichroic mirror (DMLP550R, Thorlabs), spatially co-aligned with the probe beam, and focused onto the same spot on the sample. Both pump and probe lines are focused on the sample through an optical microscope with 0.55NA/50x objective (LD EC Epiplan-Neofluar 50x/0.55 DIC M27, Zeiss) in a back-scattered configuration, passing through a half-wave plate (Thorlabs) to align the excitation polarization with the crystal axis to maximize the equilibrium Raman intensity. The sample is measured in a cryogenic-cooled cryostat (Janic Inc.) under high vacuum. Elastic scattering from the excitation line is suppressed using two volume holographic grating notch filters with $\text{OD} > 4$ (SureBlock, Coherent) in combination with a beam splitter (NoiseBlock, Coherent), enabling reliable detection of Raman shifts down to 10 cm^{-1} from the laser line.

The spectrally dispersed Raman signal is collected at the width-variable slit of the monochromator and detected using either a CCD (Synapse+, Horiba) or a single-photon avalanche photodetector (Excelitas, SPCM-AQRH-46) with additional exit slit filtering the bandwidth that enters it. Photon arrival times to the SPAD are recorded with a time-tagging module (Ultra 4 Value, Swabian Instruments), with synchronization between the laser sources, modulation electronics, and detection system provided by a Pulse Streamer 8/2 (Swabian Instruments). The time tags are recorded in 50 ps time bins, and the overall instrument temporal response function has a full-width at half-maximum of 600 ps, derived from the timing jitter of the pump laser, the electronics, the SPAD, and the diffraction grating.

A complete time-resolved Raman spectrum is obtained by sequentially scanning the monochromator grating. At

each spectral position, time-correlated single-photon counting is used to accumulate a temporal histogram of Raman photon arrival times for 20 minutes, from which the full time- and frequency-resolved Raman response is reconstructed. Average laser power used for all measurements varied between 12-30 mW for the probe laser and 12-14 mW for the pump laser.

S1.b. Silicon sample

The Silicon sample is a < 100 > cut, Boron-doped with resistivity 70-85 Ω cm which translates into dopant concentration of $\sim 1 \cdot 10^{14}$ atoms cm^{-3} (Virginia Semiconductors). The Silicon wafer has a native oxide layer.

S2. CALCULATION OF THE TIME-DEPENDENT CARRIER DENSITY

To model the spatial evolution of the charge-carrier distribution, we utilized a three-dimensional Green's function approach representing the diffusion of $N_0 = 1 \cdot 10^9$ initially excited holes, determined by the absorbed pump-pulse energy in silicon. This corresponds to an initial effective charge-carrier density of approximately $5 \cdot 10^{18}$ cm^{-3} within the first ~ 0.5 ns after excitation. The spatial distribution $n(r, z, t)$ of these carriers diffusing from a localized point source in the silicon substrate is defined by:

$$n(r, z, t) = \frac{N_0}{(4\pi Dt)^{3/2}} \exp\left(-\frac{r^2 + (z - z_0)^2}{4Dt}\right) \quad (\text{S1})$$

where $D = 12$ $\text{cm}^2 \text{s}^{-1}$ is the diffusion coefficient^{S3}, r and z are the radial and axial coordinates, and z_0 represents the initial excitation center. This center is defined by half the absorption depth of the 515 nm pump beam ($z_0 = 0.5 \alpha_{515}^{-1}$), where $\alpha_{515} = 9.25 \cdot 10^3$ cm^{-1} ^{S4}, yielding an initial excitation depth of $z_0 \approx 0.54$ μm .

The observable carrier density is calculated as an average over the effective probe volume V_{probe} , modeled using the probe-laser wavelength, microscope objective numerical aperture, and the refractive index of silicon. The instantaneous average density $\langle n(t) \rangle$ is thus determined by numerically integrating the Gaussian density distribution over a conical geometry representing the probe volume:

$$\langle n(t) \rangle = \frac{1}{V_{\text{probe}}} \iiint_{V_{\text{probe}}} n(r, z, t) dV \quad (\text{S2})$$

S3. DATA ANALYSIS

S3.a. Preliminary data treatment - background photoluminescence and noise subtraction

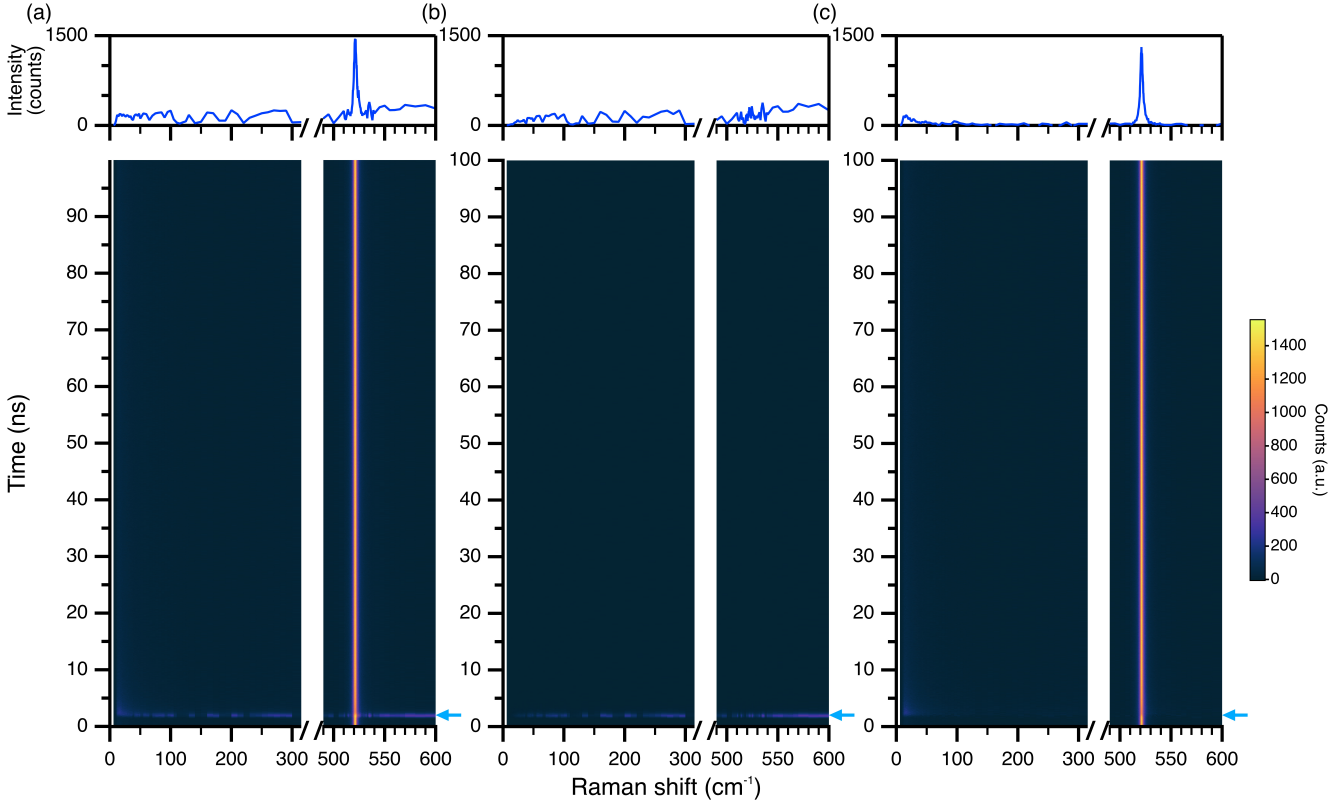


FIG. S1. Time-resolved Raman measurement scheme demonstrates the efficiency of the photoluminescence and background subtraction. Raw data at 280 K are presented as false-color heatmaps, with brighter colors indicating higher intensity. The time-resolved Raman data is collected under (a) simultaneous illumination of the pump and probe lasers and (b) under pump laser only, when the probe laser amplitude was off-modulated at the AOM. (c) The subtraction of the pump-only matrix from the pump+probe matrix yields the time-resolved Raman matrix that is used as the starting point for all subsequent analyses in this paper. Top panels - single Raman spectra reconstructed at the 2.00 ns time bin, marked with blue arrows on the heatmaps.

The raw data consist of two time-resolved Raman-spectra matrices, corresponding to the on/off modulated probe signal: one acquired with both pump and probe beams (fig. S1(a)), and one with the pump only (fig. S1(b)). Subtracting the pump-only matrix from the pump+probe matrix removes photoluminescence and other pump-induced backgrounds, as shown in the spectra at the top of the two matrices, which represent a spectrum at a specific time bin of 2.00-2.05 ns. The resulting difference matrix (fig. S1(c)) isolates the Raman background present at equilibrium, along with any additional modifications of that background not directly attributable to the pump excitation, such as electron-phonon interaction effects on the phonon lineshape. These modifications in the difference matrix are not visible to the naked eye, here specifically because they are very subtle. To that end, we define a time-smoothing window

of 10 spectra, each assigned to 50 ps, and, in total, equivalent to 500 ps, and apply a moving average throughout the time-dependent data. The time-averaged difference matrix serves as the starting point for all subsequent analyses. We extract the spectrum in the last time bin of the averaged difference matrix, referred to as the pre-excitation spectrum, and subtract it from all other time-dependent averaged spectra to get the differential spectra matrix (fig. S2).

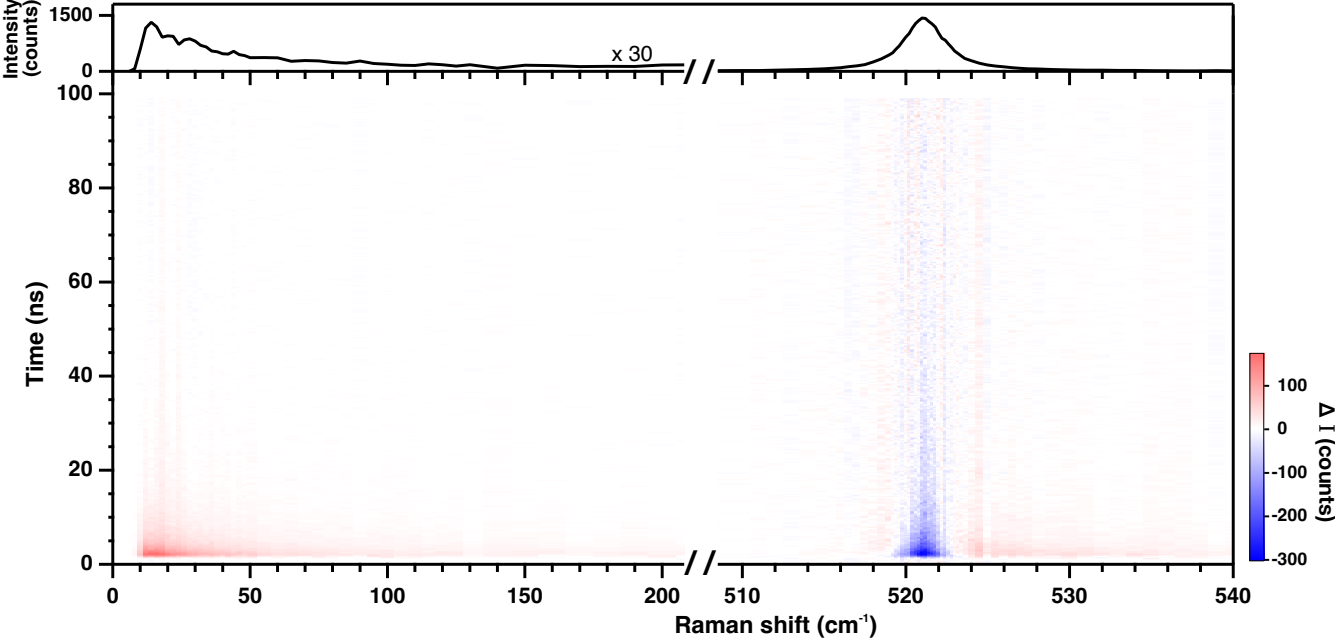


FIG. S2. Time-resolved spontaneous Raman response of lightly boron-doped silicon. Heatmap of the Stokes differential Raman intensity $\Delta I(\omega, t)$ at 280 K, defined relative to the pre-excitation spectrum (top), showing a transient low-frequency electronic continuum and a time-dependent modification of the optical phonon near 521 cm^{-1} .

S3.b. temperature-dependent integrated differential intensity

To quantify and compare the dynamics of the photoexcited effect on the two electronic transitions and the effect on the optical phonon in the studied temperature range, each differential intensity spectrum $\Delta I(\omega, t)$ was integrated over the two spectral regions associated with the carrier-induced response, namely the low-frequency *intra*-valence-band (*intra*-VB) range ($10\text{--}200 \text{ cm}^{-1}$) and the optical phonon range ($510\text{--}560 \text{ cm}^{-1}$) that is modified by interference with the *inter*-valence-band (*inter*-VB) transitions. The full time-resolved, background-subtracted differential Raman spectra matrix at 280 K is shown in fig. S2 as a false-color heatmap, where red and blue indicate signal enhancement or suppression, respectively, compared to the pre-excitation spectrum, shown in the top panel. This figure shows an example of the data used to extract the transient absolute integrated intensity. It shows a prompt response right after excitation ($t = 0 \text{ ns}$), followed by an exponential decay that almost vanishes within 30 ns, returning to the

pre-excitation spectrum. The low-frequency electronic Raman signal is amplified by the elevated density of excited charge carriers, which scatter light inelastically. The zone-center phonon around 521 cm^{-1} is distorted by coupling to the excited inter-VB transitions, as explained in the main article, showing an intensity quench at the peak (dark blue) and an increasing asymmetric signal on its higher-frequency side (light red).

The integrated differential intensity transient at each temperature was background-subtracted to eliminate different noise levels between temperatures, normalized, and fitted to a bi-exponential decay function, as shown in fig. S3 in gray curves; its results are annotated next to each decaying curve. The transients were fitted in the time range between the peak value and the first reaching the equilibrium value. The resulting temperature-dependent decay constants τ_1 and τ_2 are presented in the bottom-right corner of each subfigure. At lower temperatures ($\leq 30 \text{ K}$), the slow component is negligible, and only one decay constant is effectively dominant.

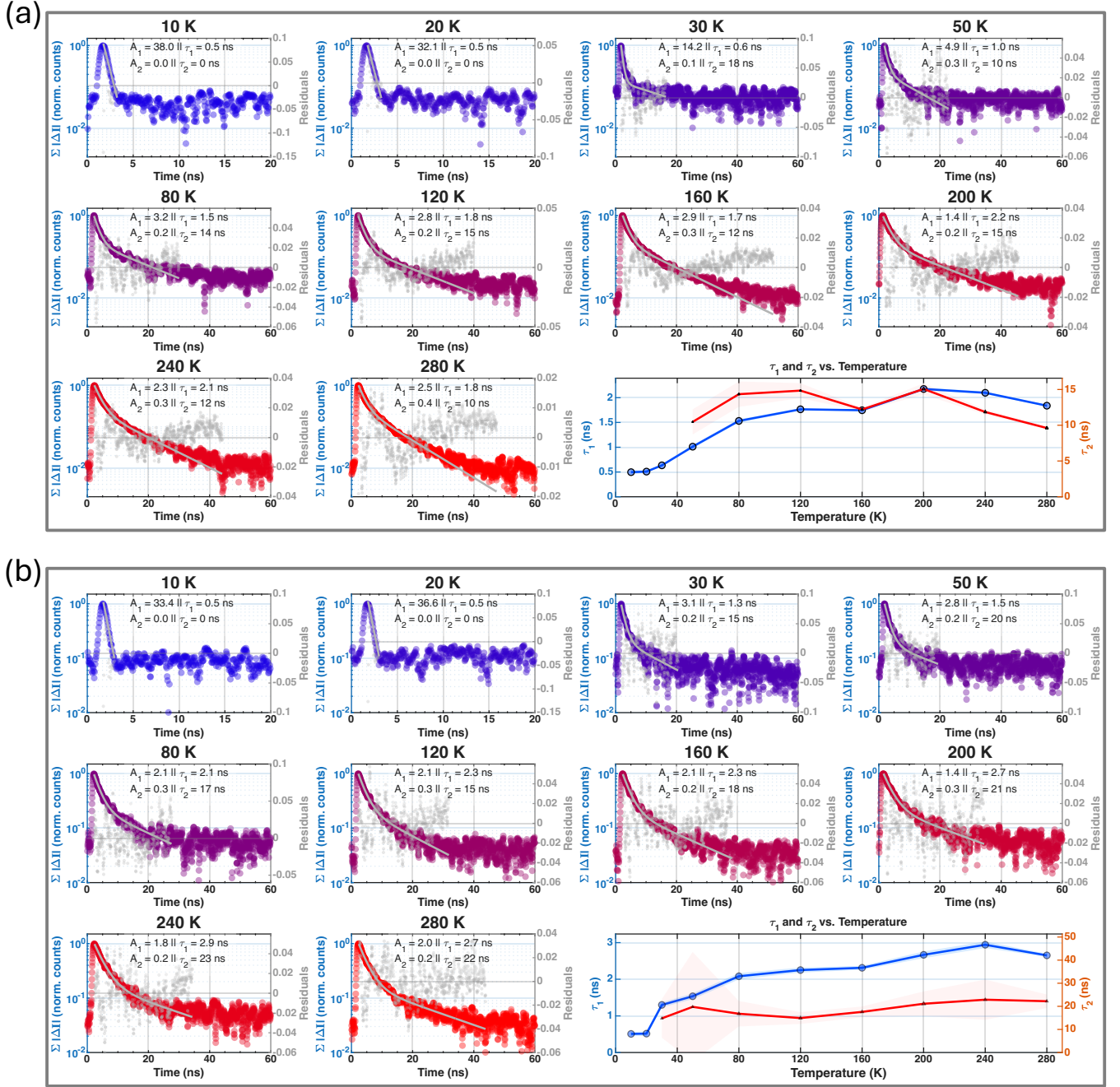


FIG. S3. Temperature-dependent integrated absolute differential intensity $\sum_{\omega} |\Delta I(\omega, t)|$ of (a) the intra-VB range and (b) the phonon range. Gray curves are the bi-exponential decay fit per transient, and gray circles are the fit residuals. The amplitude and decay constants are annotated next to the transients, and summarized at the bottom-right corners with the fast and slow decay constants plotted in blue and red, respectively. Shading represents the fit error of the decay constants, and the relative marker size represents the ratio of the fast and slow exponential amplitudes at each temperature.

S3.c. Lineshape analysis

1. Fano resonance model

The Fano interference model describes a system in which a discrete scattering state, the optical phonon, interacts through energy exchange with a continuum background of electronic transitions, here, the inter-valence band hole transitions^{S5,S6}. The temperature- and time-dependent data were fitted to a Fano lineshape of the form:

$$I = I_0 \frac{(q + \varepsilon)^2}{1 + \varepsilon^2} \quad (\text{S3a})$$

$$\varepsilon = \frac{\omega - \omega_0}{\frac{\Gamma}{2}} \quad (\text{S3b})$$

where I_0 is an intensity prefactor, q the Fano asymmetry parameter, ω the measured frequency, ω_0 the resonance frequency, and Γ the squared matrix element of the coupling between the continuum and the discrete states^{S5,S7}, experimentally correlated with the peak width. Large $|q|$ values yield a nearly symmetric lineshape, while smaller values produce pronounced asymmetry. q is proportional to the ratio of the Raman tensors for phonon and electronic scattering:

$$\Gamma q^2 \propto \left| \frac{R_{\text{phonon}}}{R_{\text{electronic}}} \right|^2 \quad (\text{S4})$$

Figure S4 shows the excited-state and equilibrium Raman spectra alongside their fit to the Fano lineshape. The fit captures the data well; a slight peak asymmetry is visible when comparing the intensities of both peak tails. The peak asymmetry is increasing with temperature, as expected from the increasing fraction of free charge carriers above 150 K due to thermal energy larger than the exciton binding energy^{S8}.

The Fano fit parameters of the excited-state spectrum are extracted for each temperature, and plotted in figure S5. The temperature trends of the resonance frequency ω_0 and the linewidth Γ are physically reasonable - the phonon resonance red-shifts and linewidth broadens with increasing temperature. On the contrary, the temperature trends of the Fano asymmetry parameter q^{-1} and the intensity prefactor I_0 are not. The Fano asymmetry factor shows a non-monotonic trend, whereas the raw data, as well as previous reports on its temperature trend in equilibrium Raman scattering, showed a monotonic, increasing trend^{S9}. This is a confirmation that in transient photodoping, the

Fano model is not physical when comparing different lattice temperatures, as it does not incorporate temperature effects^{S10,S11}.

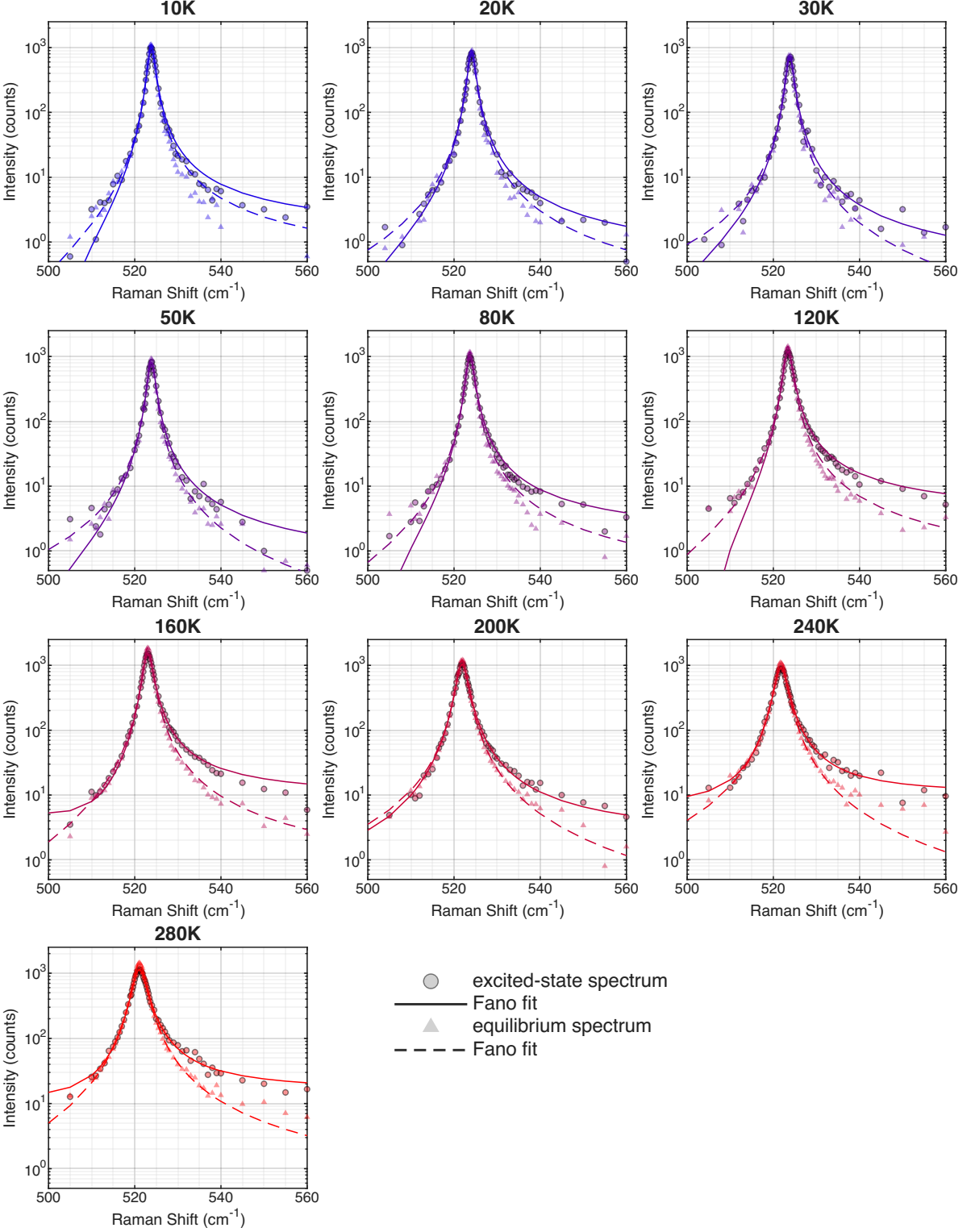


FIG. S4. Temperature-dependent Fano lineshape fit results for the excited-state (circles) and equilibrium (crosses) spectra show a good fit.

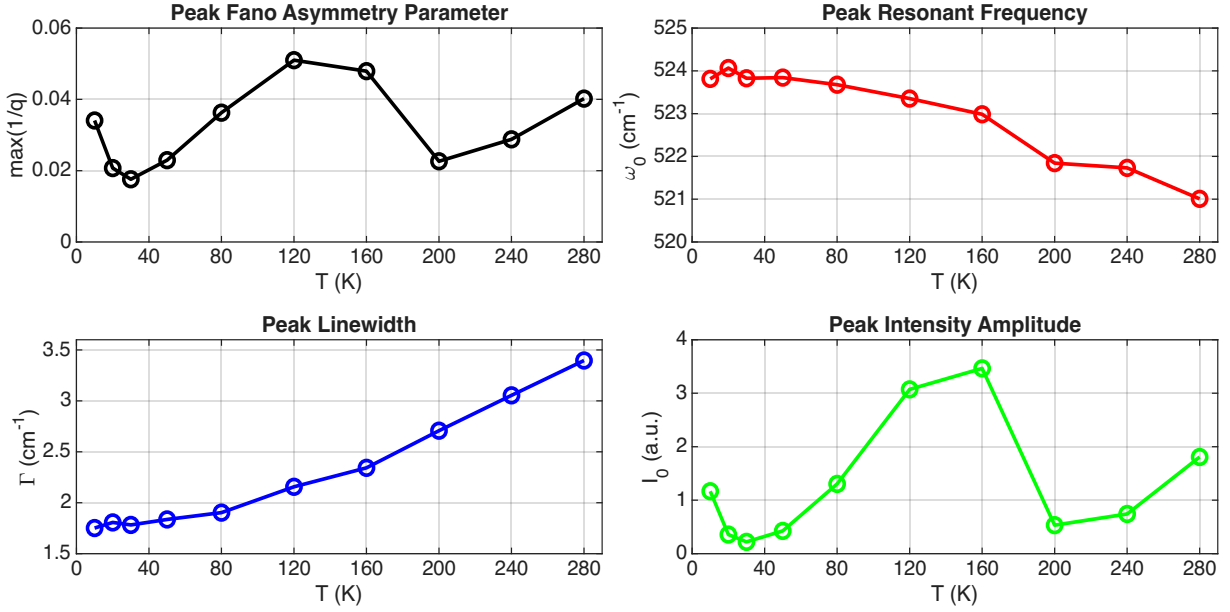


FIG. S5. Temperature-dependent Fano fit parameters extracted at the excited-state spectrum. The q^{-1} and I_0 temperature trends reveal physical anomalies.

2. Coupled-modes model analysis

The coupled-modes (CM) model, based on the single-particle Green's function $G(\Omega)$ ^{S12}, is employed to describe the interaction between vibrational modes in materials. It is beneficial for systems where vibrational states are coupled to each other. The model captures the coupling's impact on spectral features, including frequency shifts, linewidth changes, and the emergence of lineshape asymmetries.

We vary the temperature of the silicon wafer and follow the variation of the CM fit parameters. Figures S6 – S8 show the temperature-dependent transients of each CM fit parameter, with a bi-exponential decay fit for its signal decay time. We note that only for the imaginary part of the coupling, $\gamma(t)$, both low and high temperatures fitted better to a single-exponential decaying function rather than a bi-exponential; therefore, the dominant exponent was chosen at the intermediate temperatures to plot the temperature trend. As the imaginary part of the coupling term is related to the dissipation of the energy, it may have to do with the change in the dissipative channels at higher temperatures. Notably, all fit parameters are decaying faster upon cooling, where τ_1 values range between 0.3-1.5 ns (R^2), 0.6-7.4 ns (δ), and 0.6-5.0 ns (γ). The faster decay of the photoexcited effect is likely related to a change in the dominant quasiparticle dynamics associated with the formation of excitonic droplets in equivalent temperatures^{S13–S15}.

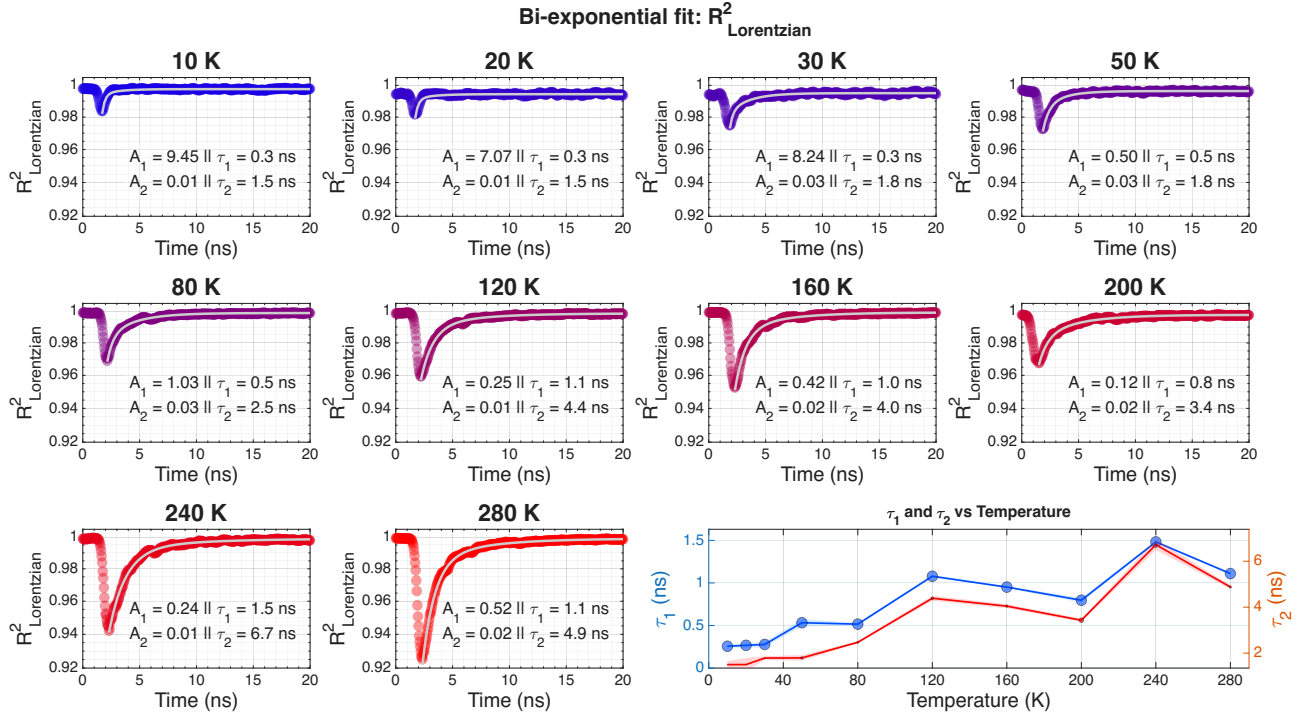


FIG. S6. Temperature- and time-dependent R^2 parameter of the Lorentzian lineshape fit tracks the temporal deviation of the spectrum from the equilibrium, Lorentzian lineshape. This quantity follows the population of excited charge carriers. All decaying curves were fitted to a bi-exponential decaying function. The bottom-right panel summarizes the time constants between 10–280 K for both τ_1 and τ_2 .

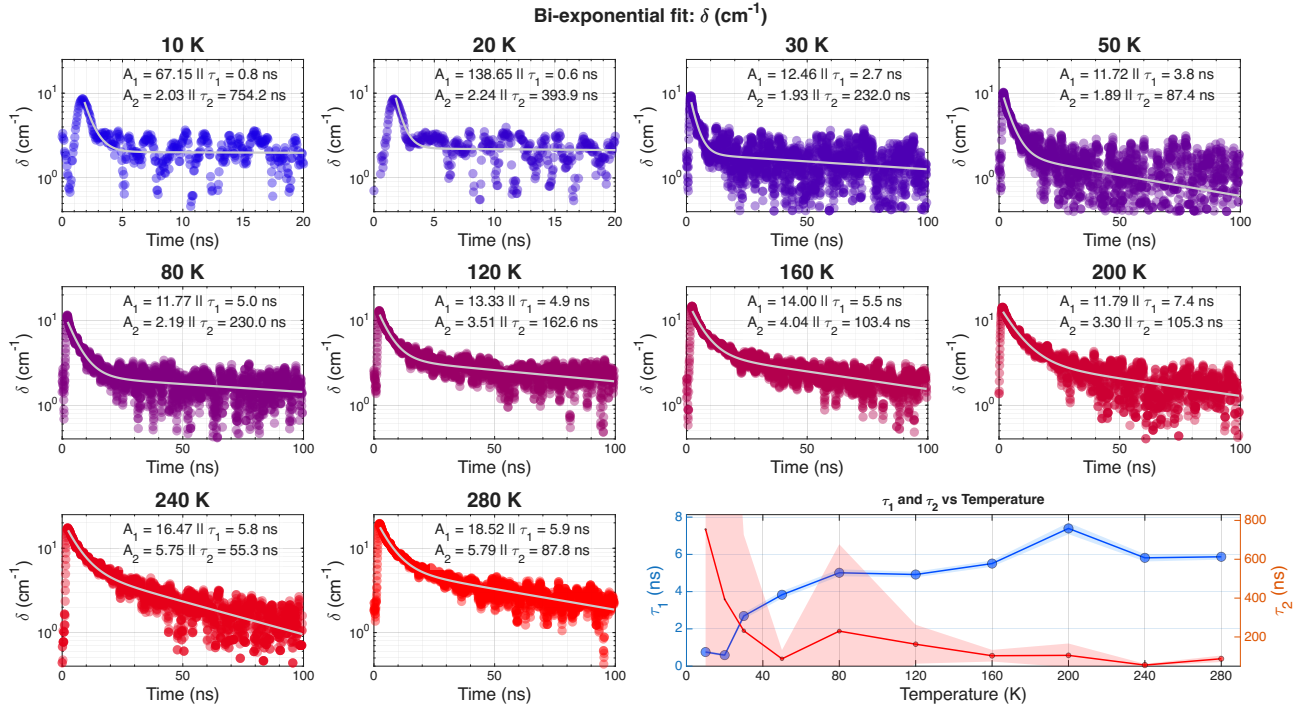


FIG. S7. Temperature- and time-dependent evolution of the coupled-modes fit parameter $\delta(t)$, the real part of the coupling term. All decaying curves were fitted to a bi-exponential decaying function. The bottom-right panel summarizes the time constants between 10–280 K for both τ_1 and τ_2 .

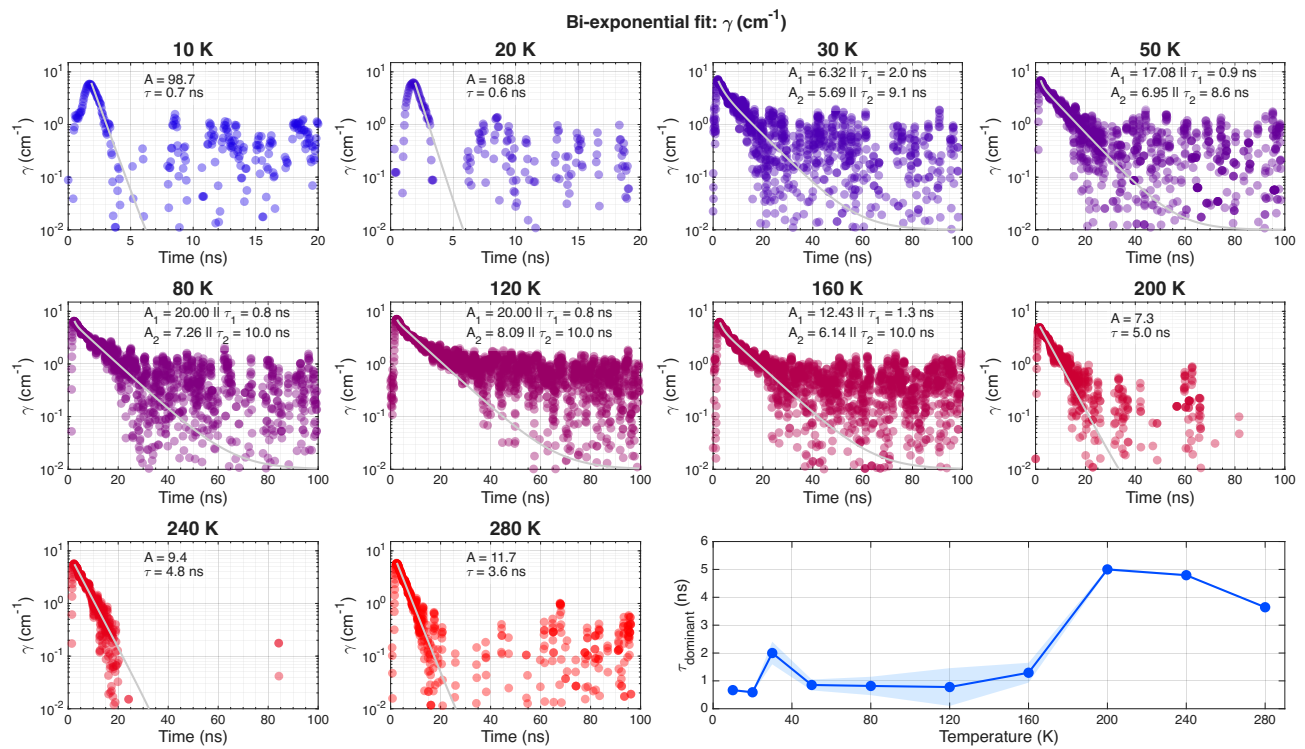


FIG. S8. Temperature- and time-dependent evolution of the coupled-modes fit parameter $\gamma(t)$, the imaginary part of the coupling term. The decaying curves were fitted to either a single- or bi-exponential decaying function, according to the best fit, and the single or dominant exponent value in the bi-exp. curves were extracted to summarize the time constants between 10–280 K.

-
- [S1] M. Asher, D. Angerer, R. Korobko, Y. Diskin-Posner, D. A. Egger, and O. Yaffe, Anharmonic lattice vibrations in small-molecule organic semiconductors, *Advanced Materials* **32**, 1908028 (2020).
- [S2] M. Menahem, Z. Dai, S. Aharon, R. Sharma, M. Asher, Y. Diskin-Posner, R. Korobko, A. M. Rappe, and O. Yaffe, Strongly anharmonic octahedral tilting in two-dimensional hybrid halide perovskites, *ACS Nano* **15**, 10153 (2021).
- [S3] S. N. Mohammad, A. V. Bemis, R. L. Carter, and R. B. Renbeck, Temperature, electric field, and doping dependent mobilities of electrons and holes in semiconductors, *Solid-state electronics* **36**, 1677 (1993).
- [S4] M. A. Green and M. J. Keevers, Optical properties of intrinsic silicon at 300 K, *Progress in Photovoltaics: Research and Applications* **3**, 189 (1995).
- [S5] U. Fano, Effects of configuration interaction on intensities and phase shifts, *Physical Review* **124**, 1866 (1961).
- [S6] B. G. Burke, J. Chan, K. A. Williams, Z. Wu, A. A. Puretzy, and D. B. Geohegan, Raman study of Fano interference in p-type doped silicon, *Journal of Raman Spectroscopy* **41**, 1759 (2010).
- [S7] F. Cerdeira, T. A. Fjeldly, and M. Cardona, Interaction between electronic and vibronic Raman scattering in heavily doped silicon, *Solid State Communications* **13**, 325 (1973).
- [S8] M. A. Green, Improved value for the silicon free exciton binding energy, *Aip Advances* **3**, 112104 (2013).
- [S9] V. Magidson and R. Beserman, Fano-type interference in the Raman spectrum of photoexcited Si, *Physical Review B - Condensed Matter and Materials Physics* **66**, 1 (2002).
- [S10] M. Balkanski, K. P. Jain, R. Beserman, and M. Jouanne, Theory of interference distortion of Raman scattering line shapes in semiconductors, *Physical Review B* **12**, 4328 (1975).
- [S11] F. Cerdeira, T. A. Fjeldly, and M. Cardona, Effect of free carriers on zone-center vibrational modes in heavily doped p-type Si. II. optical modes, *Physical Review B* **8**, 4734 (1973).
- [S12] P. C. K. Kwok, Green's function method in lattice dynamics, in *Solid State Physics*, Vol. 20 (Elsevier, 1968) pp. 213–303.
- [S13] A. Forchel, B. Laurich, J. Wagner, W. Schmid, and T. L. Reinecke, Systematics of electron-hole liquid condensation from studies of silicon with varying uniaxial stress, *Physical Review B* **25**, 2730 (1982).
- [S14] S. Revuelta and E. Cánovas, Exciton formation dynamics at the SiO₂/Si interface, *Communications Materials* **4**, 1 (2023).
- [S15] I. Pelant and J. Valenta, Luminescence of excitons, in *Luminescence Spectroscopy of Semiconductors* (Oxford University Press, Oxford, UK, 2012) pp. 161–204.